Laser & Photonics Reviews

LASER & PHOTONICS REVIEWS

www.lpr-journal.org

RESEARCH ARTICLE OPEN ACCESS

Integrated Photonic Modulator Circuit With Programmable Intensity and Phase Modulation Response

Hong Deng[1,2] | Yu Zhang[1,2] | Xiangfeng Chen[1,2] | Wim Bogaerts[1,2]

[1]Photonics Research Group, Department of Information Technology, Ghent University - imec, Ghent, Belgium | [2]Center for Nano- and Biophotonics (NB Photonics), Ghent University, Ghent, Belgium

Correspondence: Wim Bogaerts (wim.bogaerts@ugent.be)

Received: 21 October 2025 | **Revised:** 18 March 2026 | **Accepted:** 13 April 2026

Keywords: high-speed modulators | integrated photonics | silicon modulators | silicon photonics

ABSTRACT

Electro-optical modulators are essential components in optical communication systems. They encode an electrical waveform onto an optical carrier. However, their performance is often limited by inherent electro-optic processes and imperfections in existing integrated designs, which limit their adaptability to diverse applications. This paper presents a circuit-level programmable modulator design that addresses these challenges. The proposed modulator can generate both intensity and phase modulation, optimizing performance without altering the underlying design or constraining platform limitations. We explain and demonstrate the principle with both carrier depletion-based modulators and SiGe electro-absorption modulators on a silicon photonic platform. Experiments demonstrate precise control and optimization capabilities surpassing those of traditional modulator designs, marking a significant leap forward in adaptability and performance enhancement across intensity, phase, and modulation linearity, enabled by the configurable photonic circuit approach. With its built-in on-chip monitors, our circuit can be self-calibrating. This programmable modulator circuit concept can be applied to modulators in different platforms, incorporating existing phase shifter designs, and act as a drop-in replacement in more complex circuits. Designed as a platform-agnostic, modular circuit block, it has broad applicability in fields such as optical communication, LiDAR, microwave photonics, and beyond.

1 | Introduction

Electro-optical (E/O) modulators play an important role in integrated photonic systems, converting microwave signals into the optical domain by modulating the waveform onto the phase and/or amplitude of an optical carrier wave [1]. As photonic chip technologies are moving beyond the field of optical fiber communication, and into applications for optical sensing [2], LiDAR [3], and microwave signal processing (so-called microwave photonic systems [4]), the requirements on the optical modulators are also changing rapidly, including, but not limited to, larger modulation bandwidths, higher modulation efficiencies, strong linearity, and a "pure" modulation response [5, 6].

Various approaches have been proposed to achieve E/O modulators in photonic integrated circuits. For instance, in most mature silicon photonic platforms, the commonly used modulators are based on waveguides with embedded *pn* junctions, which affect the propagation of light through the free carrier dispersion effect. These *pn* junctions can be embedded in an interferometric circuit to form microring resonator modulators (MRM) and traveling-wave Mach-Zehnder modulators (TWMZM). MRMs normally have a larger electrical modulation bandwidth [7], but can only work for specific wavelengths, and also suffer from thermal drift. TWMZMs on the other hand, can be operated over a wide wavelength range, but take up a large footprint and suffer from a relatively low electrical bandwidth. Still, with a co-designed and co-packaged modulator driver, a TWMZM can also reach

a bandwidth higher than 67 GHz [8]. In parallel with pushing the bandwidth, various approaches to improve the linearity of these MRMs and TWMZMs have been pursued [9–11], using specifically-targeted custom-designed modulator building blocks. Good linearity, where the modulator does not introduce higher harmonics and nonlinear distortion of the signal, is very desirable in analog signal processing applications such as microwave photonics. Spectrum shaping is also proposed to improve the linearity of the system, but this process is quite complicated [12–14].

Apart from these carrier dispersion-based modulators mentioned above, some silicon photonics platforms also offer SiGe electro-absorption modulators (EAM) based on the Franz–Keldysh effect [15]. These devices typically have a much reduced footprint and larger modulation bandwidth. Alternative E/O modulators, such as InP (based on Franz-Keldysh or Pockels effect) [16], thin film $LiNbO_3$ on insulator (LNOI) [17, 18], thin-film $BaTiO_3$ [19] (Pockels effect), polymer modulators [20], and silicon-organic hybrids [21], can also been heterogeneously integrated onto silicon photonic circuits, with wafer-to-wafer, die-to-wafer or die-to-die bonding, or transfer-printing technologies [22]. These modulators also show promising modulation performance. However, such modulator designs are mainly explored for larger modulation bandwidth, driven by the needs for high-speed digital optical interconnects. Their performance metrics for analog signals, such as spurious intensity or phase modulation, modulation linearity and spurious-free dynamic range (SFDR), are usually far from optimal. None of these many E/O modulation mechanisms is perfect, and as different applications impose their own requirements, it is not straightforward to meet them within a single device.

In this paper, we introduce a programmable modulator design that enhances existing E/O modulators by embedding them within a fully configurable Mach-Zehnder interferometer (MZI) circuit. By tuning the static transmission response of the MZI, we can compensate for imperfections in the electro-optic response of the embedded modulator, achieving an optimized modulation response curve with benefits such as lower insertion loss, higher modulation efficiency, or improved SFDR, tailored to specific application needs. When the embedded modulator provides significant phase modulation, this circuit can be configured to function as an intensity modulator, a phase modulator, or a hybrid of both formats. This builds on prior work: we have previously reported static (DC) simulation results demonstrating pure phase modulation using a *pn* junction-based modulator [23] and its application to microwave photonic signal processing [24]. Here, we present a comprehensive experimental demonstration featuring *pn* modulators and SiGe EAMs, supported by numerical analysis. Notably, experiments with *pn* modulators achieve exceptional linearity (SFDR up to 124.6 dB $Hz^{2/3}$), pure phase modulation (spurious intensity suppressed by 20 dB), and high extinction (38 dB) across diverse operating conditions. Our modulator design serves as a platform-agnostic, modular circuit block for photonics. It is a circuit-level reusable intellectual property (IP) block can be applied to all existing photonic chip platforms that support phase shifters and E/O modulator technologies, as demonstrated through numerical simulations and analysis of a MRM. Such cross-platform circuit-level IP is still rare in integrated photonics, where performance optimization is usually handled at the building block level using full-wave Maxwell or multiphysics simulations.

Experimentally, the system-level performance improvements can be estimated from the DC response of the embedded modulator (optical phase and amplitude transmission as a function of applied voltage), which can be directly characterized within our circuit, even without prior knowledge of the modulator's design or specifications. Additionally, with on-chip thermal phase shifters and monitor photodetectors, the proposed modulator is self-calibrating, further enhancing its adaptability and ease of integration.

2 | Results

The schematic of our programmable modulator is shown in Figure 1. As can be seen, the programmable modulator is an MZI circuit formed by two tunable couplers, a high-speed modulator in one arm, a static phase shifter in the other arm, and a tap monitor. The tunable coupler itself is also an MZI consisting of two 50:50 multimode interferometer (MMI) couplers and a static phase shifter. By adjusting the phase difference between the two arms of a tunable coupler, we can adjust the power splitting ratio ($\underline{\kappa}$) between the two outputs. A monitor photodetector (tapping off a bit of light) is attached to one output port to calibrate the tunable coupler. The static phase shifters on our chip are implemented by undercut heaters [15], but could just as well be based on liquid crystal phase shifters [25] or micro-electromechanical phase shifters [26]. The two tunable couplers, together with the static phase shifter ($\underline{\phi_s}$), form an MZI structure with a fully tunable sinusoidal transmission response, which is used to compensate for the imperfections of the embedded modulator high-speed building block. This can be a *pn* junction phase modulator, an MRM, a SiGe EAM, or any other E/O modulator device.

In this work, we experimentally demonstrate the performance improvements of a *pn* junction modulator and a SiGe EAM, and use our circuit model to predict the performance improvements of an MRM on imec's iSiPP50G silicon photonic platform. The experimental setups, as well as the calibration methods, are elaborated in the Section S1. The circuit model of the modulator circuit is shown in the Section S3.

2.1 | PN Junction-Based Travelling Wave Modulator

The *pn* junction-based traveling wave modulator is one of the most commonly used modulators in silicon photonic circuits [22]. By extracting the free carriers from a silicon waveguide core, the *pn* junction can change the refractive index of the waveguide and induce a phase modulation in the guided light. However, this carrier density variance also change the insertion loss of the waveguide, resulting in a spurious intensity modulation [27]. The schematic of the *pn* junction based programmable modulator circuit is shown in Figure 2a, and a fabricated demonstrator is shown in Figure 2b. The intensity response and phase response of a fabricated 2500 μm long *pn* junction modulator is measured

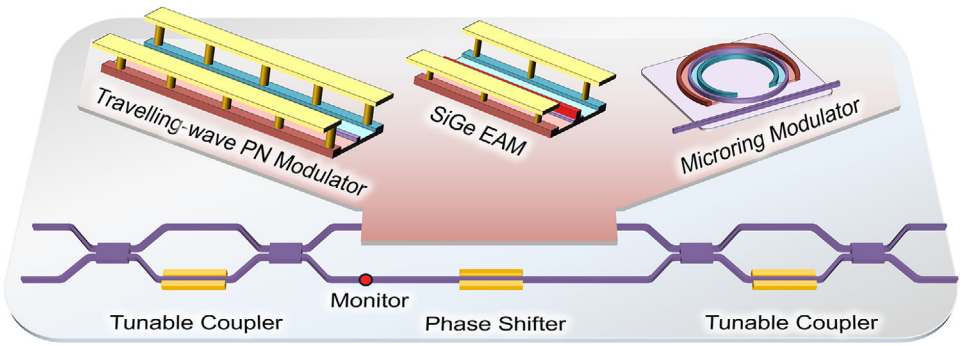

FIGURE 1 | Schematic of the programmable modulator. The embedded high-speed modulator can be travelling wave *pn* modulator, SiGe EAM modulator, microring modulator, and other modulators on silicon photonic platform or other platforms.

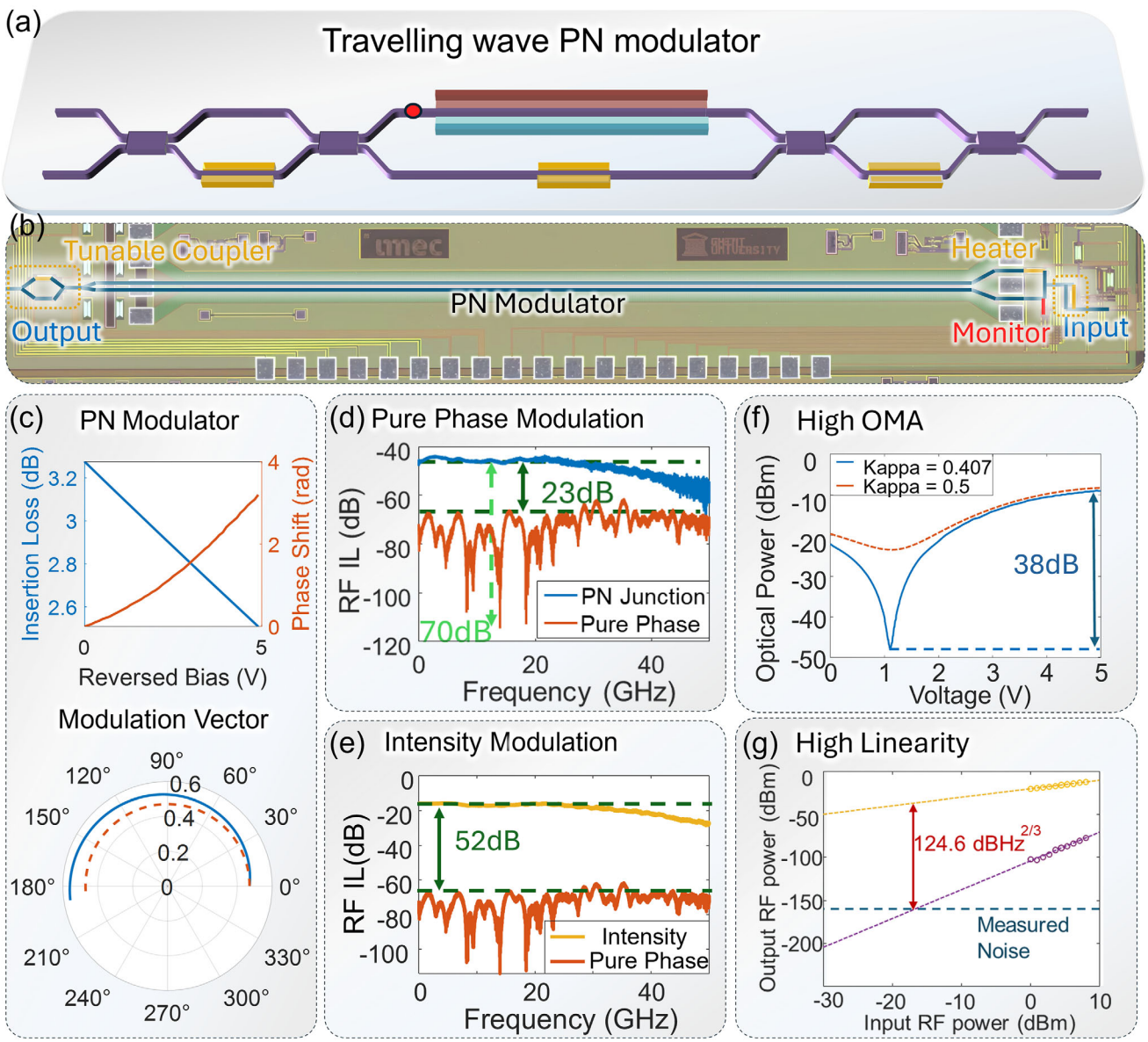

FIGURE 2 | Programmable modulator circuit based on traveling wave *pn* modulator. (a) The schematic of the modulator; (b) Fabricated demonstrator; (c) Insertion loss and the phase shift introduced by the embedded reverse biased *pn* junction;(d) S21 of the optimized pure phase modulation and the original PN junction; (e) S21 of the intensity modulation and pure phase modulation; (f) DC response of the optimized high extinction ratio modulation and a normal 50:50 MZI modulator; (g) Optimized high-linearity modulation.

as:

$$a(V) = -6.977 \times 10^{-4} V^2 + 0.160V - 3.276 \quad (1)$$

$$\phi(V) = [-7.296 \times 10^{-4} V^4 + 6.199 \times 10^{-3} V^3 + 7.404 \times 10^{-3} V^2 + 0.108V + 1.594]\pi(rad) \quad (2)$$

and the modulation curves are shown in Figure 2c.

2.1.1 | Pure Phase Modulation

The fully programmable modulator provides a tunable sinusoidal intensity response based on the phase change of the embedded *pn* junction modulator. This can be configured to have an opposite slope of the spurious intensity modulation of the *pn* junction, and eventually the intensity modulation of the entire circuit is suppressed around the operating point. The proof-of-concept measurement results are shown in Figure 2(d). When the coupling ratios of the tunable couplers are set as 0 ($\kappa = 0$), the optical carrier would be phase-modulated, and not be detected by a simple photodetector ideally. However, due to the spurious intensity modulation of the *pn* junction, an RF signal can be recovered, with an insertion loss of 45 dB. If the programmable modulator is set properly ($\kappa = 0.3, \phi_s = 1.5\pi$), this transmitted RF signal (i.e. the intensity modulation) can be suppressed by 23 dB overall, with a maximum suppression of 70 dB.

2.1.2 | High RF-Gain Intensity Modulation

The RF gain depends on the slope of the modulation curve, as well as the total optical loss. The highest RF gain is obtained when the programmable modulator is set to $\kappa = 0.48$, which balances both effects. The RF transmission response is shown in Figure 2e. From the highest RF gain intensity modulation to the lowest RF gain phase modulation, the proposed modulator shows 52 dB suppression overall, with a maximum suppression of 97 dB extinction ratio over the whole frequency range, which is superior to the reported 64 dB record (only one frequency point due to optical dispersion) using spectrum shaping [12].

2.1.3 | High Extinction Modulation

An intensity modulation with a high extinction ratio would obtain a high optical modulation amplitude, ensuring a high signal-to-noise ratio (SNR) in optical communication network and optical sensing system [2]. For an interferometer-based modulator, the extinction ratio of the modulated signal depends on the destructive interference at the optical output. However, the extra insertion loss of the embedded *pn* junction breaks the propagation loss symmetry, resulting in a low extinction ratio, if 50:50 power couplers are used. Two tunable couplers in our programmable modulator circuits can be tuned to compensate the loss imbalance of the MZI, enabling intensity modulation with high and robust extinction ratio. Experimental results are shown in Figure 2f As can be seen, when the programmable modulator is set at $\kappa = 0.407$ (around 60% light is fed into the *pn* junction), we can achieve a high extinction ratio (38 dB) in the modulator bias sweep. This result is not as good as the results shown in [2] (71 dB in the optical DC sweep, 68 dB in the RF tests), but in our case the programmable modulator will not be dependent on the optical carrier wavelength.

2.1.4 | High-Linearity Intensity Modulation

As shown in Figure 2c, the stand-alone *pn* junction shows a nonlinear phase and a nonlinear spurious intensity response. In addition, the intensity modulation is simply implemented by converting the phase modulation using an MZI, which gives a sinusoidal response and is therefore intrinsically nonlinear. With our programmable modulator circuit, we can significantly linearize the intensity modulation response by combining these two sources of nonlinearity and canceling them out. The linearity of a modulator is evaluated by its spurious-free dynamic range (SFDR). We measured the 3rd order intermodulation (IMD3) of the modulator, and the linearized result is shown in Figure 2g. The measurement setup are elaborated in the Section S1. When the programmable modulator is configured with $\kappa = 0.48$ and $\phi_s = 0.31\pi$, the SFDR is recorded at 124.6 $dBHz^{2/3}$ around a modulation frequency of 2 GHz (with a noise floor of −160.4 dBm/Hz). This performance is on par with the highest linearity silicon based modulators previously reported (123 $dBHz^{2/3}$) [10], as well as the classical bulk $LiNO_3$ MZM (123 $dBHz^{2/3}$ [12]), while maintaining a much simpler system.

2.2 | SiGe EAM Modulator

In silicon photonics, a SiGe EAM is frequently utilized as an intensity modulator due to its compact size and broad modulation bandwidth. However, it is hindered by significant insertion loss and low modulation efficiency. By integrating it into our programmable modulator circuit, we can enhance the performance of this SiGe EAM. The schematic of the modulator circuit is shown in Figure 3a, and a fabricated demonstrator is shown in Figure 3b. The characterized DC response of an independent SiGe EAM is measured as:

$$a(V) = -0.303V^2 - 0.0435V - 3.141 \quad (3)$$

$$\phi(V) = [-7.380 \times 10^{-3} V^3 + 0.1399V^2 + 1.989 \times 10^{-3} V + 0.769] \times \pi(rad) \quad (4)$$

and the modulation curves are illustrated in Figure 3c.

2.2.1 | High RF-Gain, Low Chirp Intensity Modulation

The generated RF gain depends on the modulation slope and optical insertion loss. In our programmable modulator circuit, if part of the light is directed into the other arm (not the EAM arm), the overall insertion loss of the system decreases. However, this also reduces the intensity modulation efficiency, as less light reaches the EAM. At the same time, spurious phase

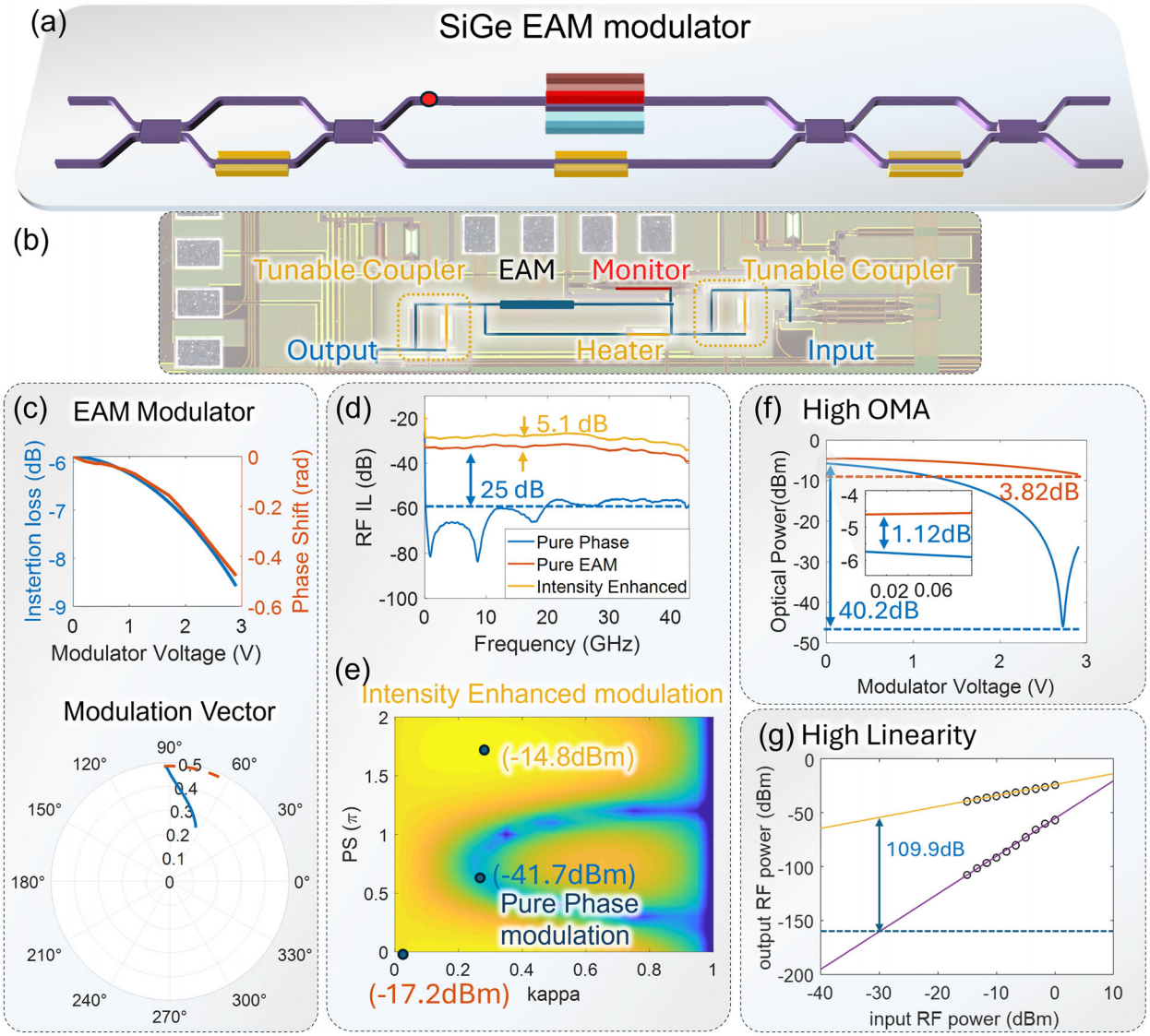

FIGURE 3 | Programmable modulator circuit based on SiGe EAM modulator. (a) The schematic of the modulator; (b) Fabricated test circuit; (c) Insertion loss and the phase shift introduced by the embedded SiGe modulator;(d) S21 of the intensity modulation, pure phase modulation and the EAM itself; (e) Measured modulated signal power with a sweep of kappa and offset phase shift; (f)DC response of the optimized high extinction modulation and a normal SiGe modulator; (g) Optimized high-linearity modulation.

modulation, although very weak, can be partially converted into intensity modulation, resulting in a lower chirp. Figure 3d compares the S_{21} responses of the embedded EAM ($\kappa = 0$), the high RF-gain configuration ($\kappa = 0.3$ and $\phi_s = 1.9\pi$), and the pure phase modulation configuration ($\kappa = 0.3$ and $\phi_s = 0.6\pi$)). As shown, the modulator circuit achieves a 5.1 dB gain improvement in the high-gain setting. What should be noted is that, the insertion loss of the programmable modulator is 0.6 dB lower than that of a standalone SiGe EAM, also contributing to the RF gain enhancement. This improvement is also evident when a single-tone signal is fed into the modulator, and the RF output is monitored from the photodetector, as illustrated in Figure 3(e).

Furthermore, we observed that the pure phase modulation point nearly aligns with the null points of the MZI, due to the limited phase modulation range of the EAM. As a result, it is not sufficient for achieving effective phase modulation.

2.2.2 | High Extinction Intensity Modulation

SiGe EAMs also suffer from low modulation extinction. Taking advantage of the phase modulation of the EAM, our programmable modulator can be set to have a high-extinction-ratio modulation. Experimental results in Figure 3f show that the optical intensity variance can reach 40 dB extinction ratio within the applied voltage range, which is 36 dB higher than a single SiGe EAM (3.82 dB at 1550 nm), with an 1.12 dB extra insertion loss (at 0 V) as a trade-off.

2.2.3 | High-Linearity Intensity Modulation

As shown in Figure 3b, the intensity response is also not linear. Our programmable modulator circuits can also improve linearity. Experimental results in Figure 3g show that the SFDR of the system can be boosted to 110 dBHz$^{2/3}$ ($\kappa = 0.55, \phi_s = 0.9\pi$), which is

around 22 dB higher than the standalone SiGe EAM (88 $dBHz^{2/3}$, biasing at 0.5 V). In other tests, the EAM SFDR can be improved from 102.8 to 112.5 $dBHz^{2/3}$ when biasing at 1 V, or 109 improved to 114.5 $dBHz^{2/3}$ when biasing at 2 V. Compared with previously reported results [28, 29], our programmable modulator shows higher SFDR and better linearity optimization. More details are listed in the Supplementary information S3.

2.3 | Microring Resonator Modulator

Previous experimental results show the optimization possibilities of the proposed programmable modulators. Another commonly used optical modulator in the silicon photonics platform is the microring modulator (MRM), known for its compact size, low power consumption, and high operational bandwidth. However, it can only work close to its resonance wavelength, and its intensity modulation is quite nonlinear. Here, we extract the DC responses of an MRM fabricated in the imec ISIPP50G platform, develop a quasi-static model of the MRM, and simulate its RF responses when embedded within our programmable modulator. At the time of writing, we have not implemented experimental circuits for the MRM.

As a cavity, an MRM exhibits different responses at varying wavelengths [30]. The fabricated MRM was measured with a Q-factor of 2212.1 and a resonance wavelength of 1556.424 nm. For the simulation, we set the operating wavelength to 1556.2488 nm, where the MRM generates the strongest RF signal. The measured MRM modulation responses of the MRM at this wavelength are shown in Figure 4b. More details about the MRM characterization is shown in Section S2.

2.3.1 | High RF-gain Intensity Modulation

To simulate the RF response using our MRM model, we applied a sinusoidal waveform with an amplitude of 1 V and a bias voltage of −1 V as the input RF signal for the MRM. By sweeping the optical wavelength, we identified 1556.2488 and 1556.655 nm, which yielded the highest optical sidebands. These wavelengths are located on opposite sides of the resonant wavelength. At these points, the optical phase variation exhibits opposite behavior: one phase increases with a higher reverse bias voltage, while the other decreases with the same voltage increase. Here we used 1556.2488 nm as the carrier wavelength for these simulation analysis.

To further improve the RF-gain, we can embed the MRM in the proposed programmable modulator. By setting $\kappa = 0.13$ and $\phi_s = 0.828\pi$, we can pump up the generated RF signal by another 0.5 dB, as shown in Figure 4c.

2.3.2 | Low-Chirp Intensity Modulation

As shown in Figure 4b, intensity modulation from an MRM would also come with phase modulation, which would also introduce frequency chirping in the modulated light signal. Here again, we can set our programmable modulator with kappa and offset phase, thus the phase change can be reduced from from 0.3585 to 0.1109 rad in the bias range of 6 V, and the intensity variance can also be improved from 4.0547 to 11.3301 dB, while trade off a 5 dB higher insertion loss when the MRM is biased at 0 V, as shown in Figure 4d.

2.3.3 | Pure Phase Modulation

Oppositely, we can also set the programmable modulator with $\kappa = 0.32$ and $\phi_s = 1.94\pi$. At this operation point, the intensity variance is reduced from 4.0547 to 0.0664 dB in the reversed voltage range of 6 V, while the phase variance can even be improved from 0.3585 to 0.7545 rad, as shown in Figure 4(d).

2.3.4 | High Extinction Intensity Modulation

As an optical cavity, the designed MRM can already provide a high extinction intensity modulation. The measured extinction ratio of the fabricated MRM is around 26 dB. While, in the simulation, we can precisely set the programmable modulator ($\kappa = 0.3372$ and $\phi_s = 1.638\pi$) to have an infinite extinction, where the embedded MRM can only provide 16.5 dB (optical carrier is at 1556.454 nm at the moment), as shown in Figure 4e. But this operation would introduce around 7 dB extra optical insertion loss as a trade-off.

2.3.5 | High-Linearity Intensity Modulation

The linearity of the MRM highly depends on the optical signal wavelength for the modulation, and it is also quite limited, due to its Lorentzian filtering response. As discussed above, we set the optical wavelength at 1556.2488 nm to ensure the highest RF gain. From the simulation, we can find out that, when programmable modulator is set at $\kappa = 0.35$ and $\phi_s = 0.414\pi$, the SFDR can be improved around 10 dB, with an 3.7 dB lower RF gain, as shown in Figure 4h.

3 | Discussion

Our programmable modulator circuit embeds the high-speed modulator into a tunable MZI structure and leverages both the static MZI response and the high-speed phase (or intensity) response to optimize the intensity (or phase) response of the embedded modulator. With these enhancements, the high-speed performance (3 dB bandwidth) remains unchanged. As demonstrated earlier, the performance improvements are significant, as summarized in Table 1, though certain constraints and opportunities for further optimization remain.

3.1 | Large Signal Performance

Due to the low modulation efficiency of silicon photonic modulators, they typically require large RF drive signals. This requirement may limit the optimization performance of the proposed programmable modulator. Here, we revisit the PN junction-based programmable modulator as an example. As previously discussed, its spurious intensity modulation can be effectively

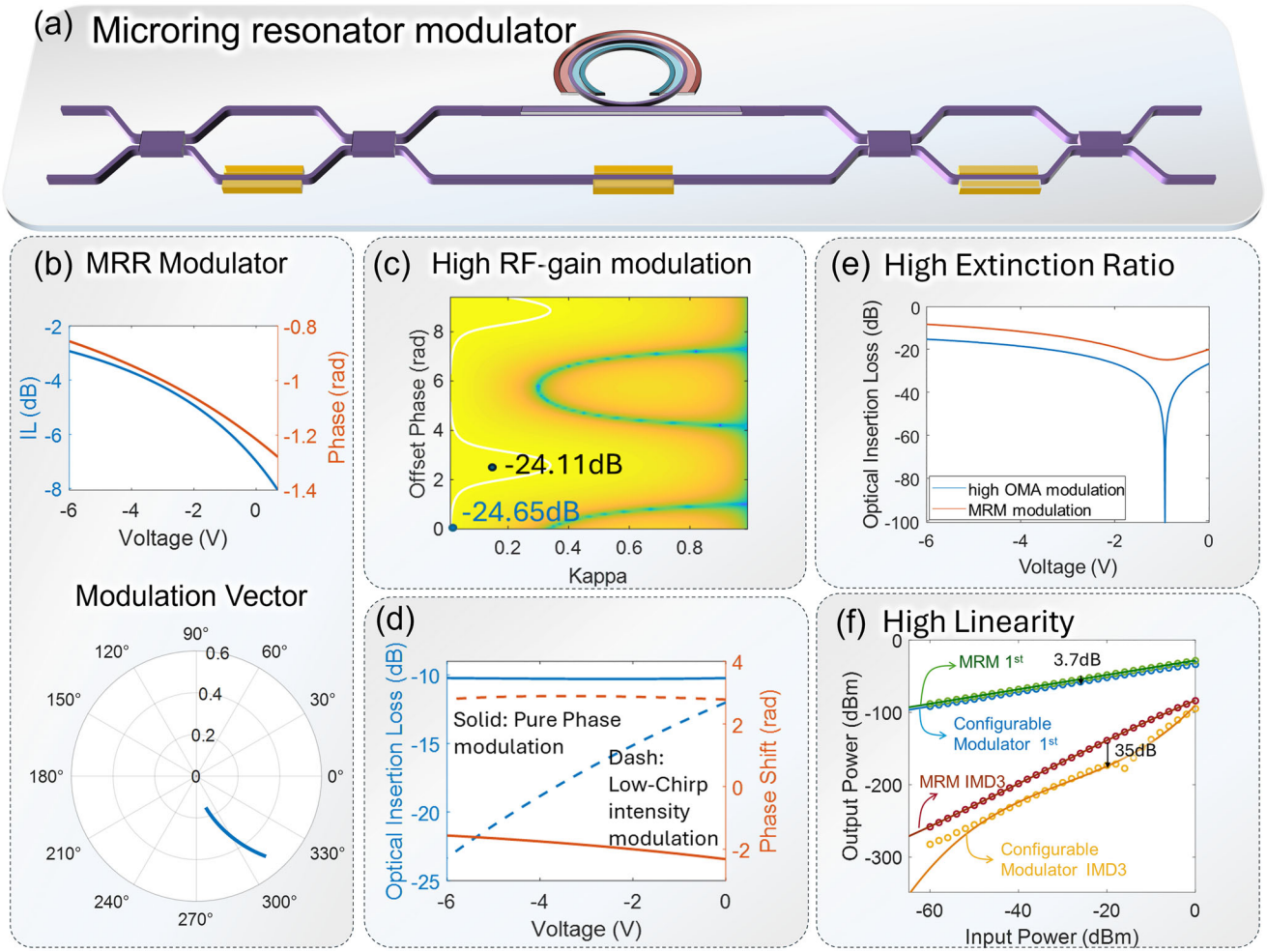

FIGURE 4 | Programmable modulator based on a microring modulator. (a) The schematic of the modulator; (b) Insertion loss and the phase shift introduced by the embedded microring modulator.

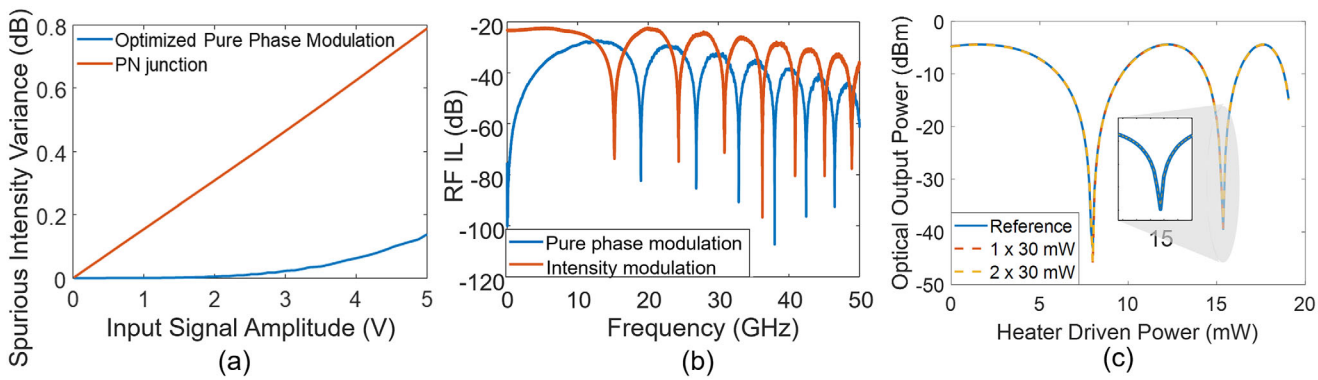

FIGURE 5 | (a) Large signal analysis, with PN junction based programmable modulator for pure phase modulation; (b) Pure phase modulation verification, two microwave photonic filters with programmable modulator and 25 km fibers. (c) Thermal crosstalk analysis.

suppressed. Figure 5a presents the simulated intensity variance as a function of input power for the programmable modulator with a PN junction and the embedded PN junction. The results demonstrate that while the optimization effect diminishes with increasing input signal power, it still provides a noticeable performance enhancement.

3.2 | Pure Phase Modulation Verification

We demonstrated that, under specific configurations, our programmable modulator is capable of delivering pure phase modulation with minimal intensity variation. However, direct detection of the light's phase variance is not feasible using standard

TABLE 1 | Proposed modulator circuit performance.

Modulator circuit		Spurious IM (dB)[c]	RF gain (dB)	Extinction (dB)	SFDR ($dBHz^{2/3}$)
Si PN depletion based	Performance[a]	<−70	−18	38	124.6
	Improved[b]	−23	0.7	21.5	15 dB
SiGe EAM based	Performance[a]	<−41.7	−26.6	40.2	109.9
	Improved[b]	—	5.1	36.38	22 dB
MRM based (simulation)	Improved[b]	−40	0.5	80	10 dB
Bulk LN Modulator [12]	Performance	>−64	1.2	>20	123
Microring Modulator [2]	Performance	—	—	71	—
Si PN-Junction [31]	Performance	—	−19.5	45	92
SiGe EAM [29]	Performance	—	−20	45	82

[a]The optimized configuration is different for the metrics.
[b]Compared with the embedded modulator.
[c]Lower is better.

photodiodes. To address this, we employed a 25 km optical fiber, leveraging its dispersion to create a two-tap microwave photonic filter [32]. The filtering results are presented in Figure 5b. The two filter responses are interleaved, revealing that the light signals exhibit phase modulation and intensity modulation, respectively. This confirms the ability of our programmable modulator to operate as a broadband RF filter with a tunable extinction ratio, achieving a maximum of 80 dB.

3.3 | Optical Length Matching

Another factor that can influence the optimization behavior is the optical length balance in the proposed programmable modulator. However, perfect balance between the two arms of the modulator is not achievable due to the asymmetric optical design, where one arm contains the modulator while the other does not. We designed our circuits in a symmetric way, but it still shows some dispersion introduced by the optical delay difference. This dispersion would add extra phase difference in the optical modulated sidebands, distorting the setting points needed of the programmable modulator circuits. And this is also the reason why, in Figure 5b, the maximum points of the intensity modulation cannot fully match the minimum points of the phase modulation.

3.4 | Thermal Crosstalk

Our demonstrators for the modulators configurations are based on the tuning of our thermal optical phase shifts, which needs extra driven electrical powers and introduced thermal crosstalk (main contributing to the phase mismatch between simulation and experimental results). To reduce this crosstalk, the thermal phase shifters we used in the demonstrators are enhanced with a local substrate undercut, which help increasing the thermal efficiency and reducing the thermal crosstalk simultaneously. We tested the thermal efficiency and crosstalk of the heaters. First, we swept the driving power applied to a phase shifter in a tunable coupler and monitored the optical output. Next, we activated a neighboring phase shifter with 30 mW of power and repeated the sweep, followed by activating an additional neighboring phase shifter and performing the sweep once more. The resulting optical power traces are plotted in Figure 5c. As shown, the phase shifter demonstrates a thermal efficiency of 3.68 mW/π, and the crosstalk effects on the coupling ratio are negligible.

An alternative way is that the circuits can be designed and fabricated statically with the specific parameters that match the desired optimized configuration. Like in ref. [33], a switch was proposed for no residual amplitude modulation, and it was specifically designed and fabricated with optimized parameters which are discussed in Section 2.1 in this paper. Additionally, innovative approaches such as phase-changing materials, MEMS, or liquid crystal materials might be employed here to achieve low power consumption and minimal thermal crosstalk in optical phase tuning.

3.5 | Modulator Linearization

Modulator linearization strategies have evolved rapidly in recent years, with increasing emphasis on reshaping either the optical carrier or the generated modulation sidebands to suppress nonlinear distortion [12, 34–36]. Conceptually, the present work operates by directly tuning the modulator transfer function on the optical carrier. Compared with previous arts, such as using on-chip stimulated Brillouin scattering (SBS) to linearize a dual-parallel MZM [36], the proposed modulator circuit offers distinct advantages. SBS operates effectively only within a limited frequency range defined by the Brillouin gain bandwidth, and the resulting phase and amplitude responses are intrinsically coupled through the Kramers–Kronig relations. Furthermore, SBS typically requires high optical pump power and specialized nonlinear materials. In contrast, our approach utilizes tunable balanced MZIs to deterministically tailor the optical carrier, avoiding both bandwidth constraints and Kramers-Kronig coupling.

In our experiment, the modulated signal probes are around 2 GHz. Because the IMD signals are significantly weaker than the fundamental tones, multiple cascaded electrical amplifiers were employed to sufficiently amplify the signal for reliable

detection. Lower-frequency amplifiers generally offer lower cost, higher gain, and improved noise performance compared to their broadband or high-frequency counterparts. For this reason, a modulation frequency of 2 GHz was selected as a trade-off between measurement reliability and system complexity. But our scheme only tunes the static modulator configurations, and the used MZI structures are balanced ones (so, no FSR distortion), thus the linearization optimization can equivalently operated at higher frequencies.

3.6 | Summary

This paper presents a programmable modulator circuit optimized via static phase shifters, with the embedded modulator as the only high-speed component, preserving its 3 dB bandwidth across configurations. Its simple design ensures simulation-experiment alignment, universal compatibility with photonic platforms, and demonstrated versatility with traveling-wave *pn* junction and SiGe EAM modulators, suggesting broad applicability in optical communication, LiDAR, and microwave photonics.

4 | Methods

4.1 | Silicon Chip Fabrication

The measured modulators were fabricated in the imec iSiPP50G silicon photonic platform on 200 mm wafers, in which 30 GHz PN junction based modulators, 50 GHz MRM, and 50 GHz SiGe EAM are provided. The circuit link is simulated using Luceda circuit analyzer, and the chip layout is designed by Luceda IPKISS.

4.2 | System Driving and Characterization

In our demonstrations, the thermal phase shifters, the tap monitors, and the modulator DC bias, are driven by source meters (Keithley 2401). The optical carrier is provided by a tunable laser source (Santec TSL550), and the recovered RF signal is generated by a 42 GHz PD (Discovery LabBuddy DSC10H, 43 GHz). The RF response of the optical link is measured by a vector network analyzer (Keysight E8364B, 50 GHz). The RF signal sources for the SFDR tests are two signal generators (Rohde&Schwarz SMR 40) and the used electrical spectrum analyzer is a Keysight EXA signal analyzer (N9010A 44 GHz). The whole characterization system and more details are shown in Section S1.

4.3 | System Calibration and Tradeoffs

To mitigate sensitivity to fabrication variations, the proposed circuit supports self-calibration with dedicated optical power monitors. Dedicated optical power monitors (photodetector) are placed after the tunable couplers. By mapping the applied driving power to the normalized monitor output power, the effective coupling ratio of each tunable coupler can be accurately extracted and calibrated. This procedure ensures that the target operating point and overall circuit performance are maintained despite fabrication variations. Similar calibration strategies have been demonstrated in our earlier works [24, 37].

Optical phase shifters play an important role in our programmable modulator design. The imec iSiPP50G silicon photonic platform provides doped silicon heater with undercut process, enjoying high thermal efficiency and low thermal crosstalk. The other required building blocks–waveguides, 2 × 2 MMIs, and optical phase shifters–are all standard components in mainstream silicon photonics process design kits (PDKs), introducing minimal integration complexity. The extra components introduce an optical insertion loss of approximately 0.28 dB per tunable coupler [37]. Thermal phase shifters require a tuning power of 3.68 mW/π, resulting in an average extra power consumption of 11.04 mW for the circuit.

4.4 | Embedded Modulator Characterization

The performance of the programmable modulator is determined by the embedded E/O modulator, as well as the splitting ratio of the tunable couplers (which can be tuned from 0 to 1) and the offset phase shift (which can be set between 0 to 2π). Thus, the characterization of the embedded E/O modulator is critical.

The embedded modulator can be directly characterized using the proposed programmable modulator. The reference performance can be obtained by setting the splitting ratio of the tunable couplers to 1, ensuring no light is fed into the embedded modulator. Conversely, the intensity response of the embedded modulator can be measured by setting the tunable couplers to 0, directing all light into the embedded modulator. We can then configure the tunable couplers to a 50:50 ratio to form a Mach–Zehnder interferometer and use the interference behavior, along with the previously extracted intensity response, to fit the phase response of the embedded modulator. This method indicates that our programmable modulator can also be designed to characterize an unknown optical components.

4.5 | Modulator Linearization

The transmission of the programmable modulator circuit as [23]:

$$E_{\text{output}} = [\sqrt{(1-\kappa_1)(1-\kappa_2)}\alpha(V)e^{-j\phi_m(V)} + \sqrt{\kappa_1\kappa_2}e^{-j(\phi_s-\pi)}]E_{\text{input}} \tag{5}$$

where κ_1 and κ_2 are the coupling ratios of the splitter and combiner, $\alpha(V)$ and $\phi_m(V)$ represent the intensity and phase responses of the embedded modulator, respectively, and ϕ_s is the offset phase difference between the modulator arm and the other. It can be found that κ_1 and κ_2 are interchangeable.

To simplify the synthesis, we assumed that the modulator is a pure phase modulator. When the modulator is modulated by a two-tone signal V_{in}, then $\alpha(V) = \alpha$ and $\phi_m(V)$ is:

$$\begin{aligned}\phi_m(t) &= \frac{\pi}{V_\pi}V_{in}(t)\\ &= \frac{\pi}{V_\pi}V_{RF}(\cos\omega_1 t + \cos\omega_2 t)\\ &= m(\cos\omega_1 t + \cos\omega_2 t)\end{aligned} \tag{6}$$

where V_π is the voltage needed for π phase shift from the modulator, ω_1 and ω_2 are the two tone signal with an amplitude of V_{RF}, and $m = (\pi / V_\pi)V_{RF}$.

Using the Jacobi–Anger expansion,

$$\begin{aligned} e^{-j\phi_m(t)} &= e^{-jm(\cos\omega_1 t+\cos\omega_2 t)} \\ &= e^{-jm\cos\omega_1 t}e^{-jm\cos\omega_2 t} \\ &= \sum_{p=-\infty}^{\infty}\sum_{n=-\infty}^{\infty}(-j)^{p+n}J_p(m)J_n(m)e^{-j(p\omega_1+n\omega_2)t} \end{aligned} \tag{7}$$

Assuming the light signal $E_{\text{input}} = e^{-j(\omega_c t)}$ is modulated, and the tunable couplers are set as $\kappa_1 = \kappa_2 = \kappa$ the output field can be expressed as

$$E_{\text{output}}(t) = e^{j\omega_c t}\left[(1-\kappa)\alpha\sum_{p,n}(-j)^{p+n}J_p(m)J_n(m)e^{-j(p\omega_1+n\omega_2)t} - \kappa e^{-j\phi_s}\right] \tag{8}$$

so, the optical carrier amplitude can be expressed as:

$$E_c = (1-\kappa)\alpha J_0^2(m) - \kappa e^{-j\phi_s} \tag{9}$$

and the sidebands amplitude is

$$E_{p,n} = (-j)^{p+n}(1-\kappa)\alpha J_p(m)J_n(m) \tag{10}$$

When the modulated optical light are detected by a photodiode, the output electrical signal is:

$$I_{pd}(t) = E_{\text{output}}(t) * E^*_{\text{output}}(t) \tag{11}$$

if the first three orders of sidebands are taken into account, $2\omega_1 - \omega_2$ signal (one of the IMD3 signal) can be expressed as:

$$\begin{aligned} I_{\text{IMD3}}(t) &\approx E_0^* E_{2,-1} + E_{1,0}^* E_{3,-1} + E_{0,-1}^* E_{2,0} \\ &= -j(1-\kappa)\alpha\kappa J_1(m)J_2(m)e^{-j\phi_s} - (1-\kappa)^2\alpha^2 J_0(m)J_1^2(m)J_3(m) \end{aligned} \tag{12}$$

Thus, when the coupling ratio of the tunable couplers κ and phase shifter ϕ_s match the condition:

$$\kappa e^{-j\phi_s} = j(1-\kappa)\alpha\frac{J_0(m)J_1(m)J_3(m)}{J_2(m)} \tag{13}$$

The IMD3 signals would be suppressed.

It should be noted that the real modulators absorption loss $\alpha(V)$ do varies with the input RF signal, then the best linearization operation point drifts from the condition in Equation (13). With the fully characterized modulator performance, numerical simulations can reveal the best configuration points directly and precisely, which is shown in Supplementary Materials Section S3.

Acknowledgements

The research presented here was supported by the European Research Council through the Consolidator Grant PhotonicSWARM (grant 725555), and the European Horizon2020 program through the projects MORPHIC (grant 780283)

Conflicts of Interest

The author declare no conflicts of interest.

Data Availability Statement

Data sharing not applicable to this article as no datasets were generated or analysed during the current study.

References

1. G. T. Reed, G. Mashanovich, F. Y. Gardes, and D. J. Thomson, "Silicon Optical Modulators," *Nature Photonics* 4, no. 8 (2010): 518–526.

2. Z. Cheng, X. Shu, L. Ma, et al., "On-Chip Silicon Electro-Optical Modulator With Ultra-High Extinction Ratio for Fiber-Optic Distributed Acoustic Sensing," *Nature Communications* 14, no. 1 (2023): 1–9.

3. K. Sayyah, R. Sarkissian, P. Patterson, et al., "Fully Integrated FMCW LiDAR Optical Engine on a Single Silicon Chip," *Journal of Lightwave Technology* 40, no. 9 (2022): 2763–2772.

4. H. Feng, T. Ge, X. Guo, et al., "Integrated Lithium Niobate Microwave Photonic Processing Engine," *Nature* 627, no. 8002 (2024): 80–87.

5. D. Thomson, A. Zilkie, J. E. Bowers, et al., "Roadmap on Silicon Photonics," *Journal of Optics* 18, no. 7 (2016): 073003.

6. S. Shekhar, W. Bogaerts, L. Chrostowski, et al., "Roadmapping the Next Generation of Silicon Photonics," *Nature Communications* 15, no. 1 (2024): 1–15.

7. H. Li, B. Casper, G. Balamurugan, et al., "A 112 Gb/s PAM4 Silicon Photonics Transmitter with Microring Modulator and CMOS Driver," *Journal of Lightwave Technology* 38, no. 1 (2020): 131–138.

8. K. Li, D. J. Thomson, S. Liu, et al., "An Integrated CMOS–Silicon Photonics Transmitter With a 112 Gigabaud Transmission and Picojoule per bit Energy Efficiency," *Nature Electronics* 6, no. 11 (2023): 910–921.

9. S. Chen, G. Zhou, L. Zhou, L. Lu, and J. Chen, "High-Linearity Fano Resonance Modulator Using a Microring-Assisted Mach-Zehnder Structure," *Journal of Lightwave Technology* 38, no. 13 (2020): 3395–3403.

10. H. Yu, P. Xia, Q. Zhang, Z. Fu, X. Wang, and J. Yang, "High Linearity Silicon Modulator Capable of Actively Compensating Input Distortion," *Optics Letters* 45, no. 13 (2020): 3785–3788.

11. C. G. Bottenfield, V. A. Thomas, and S. E. Ralph, "Silicon Photonic Modulator Linearity and Optimization for Microwave Photonic Links," *IEEE Journal of Selected Topics in Quantum Electronics* 25, no. 5 (2019) 1–10, https://doi.org/10.1109/JSTQE.2019.2908784.

12. O. Daulay, G. Liu, K. Ye, et al., "Ultrahigh Dynamic Range and low Noise Figure Programmable Integrated Microwave Photonic Filter," *Nature Communications* 13, no. 1 (2022): 1–8.

13. X. Guo, Y. Liu, T. Yin, et al., "Versatile Silicon Microwave Photonic Spectral Shaper," *APL Photonics* 6, no. 3 (2021): 36106.

14. G. Liu, O. Daulay, Y. Klaver, et al., "Integrated Microwave Photonic Spectral Shaping For Linearization and Spurious-Free Dynamic Range Enhancement," *Journal of Lightwave Technology* 39, no. 24 (2021): 7551–7562.

15. F. Ferraro, P. De Heyn, M. Kim, et al., "Imec Silicon Photonics Platforms: Performance Overview and Roadmap," 12429 (2023): 22–28, https://doi.org/10.1117/12.2650579.

16. P. Pintus, Z. Zhang, S. Pinna, et al., "Characterization of Heterogeneous InP-on-Si Optical Modulators Operating Between 77 K and Room Temperature," *APL Photonics* 4, no. 10 (2019): 100805.

17. C. Wang, M. Zhang, X. Chen, et al., "Integrated Lithium Niobate Electro-Optic Modulators Operating at CMOS-Compatible Voltages," *Nature* 562, no. 7725 (2018): 101–104.

18. T. Vanackere, T. Vandekerckhove, L. Bogaert, et al., "Heterogeneous Integration of a High-Speed Lithium Niobate Modulator on Silicon Nitride Using Micro-Transfer Printing," *APL Photonics* 8, no. 8 (2023): 86102.

19. F. Eltes, C. Mai, D. Caimi, et al., "A BaTiO3-Based Electro-Optic Pockels Modulator Monolithically Integrated on an Advanced Silicon Photonics Platform," *Journal of Lightwave Technology* 37, no. 5 (2019): 1456–1462.

20. I. Taghavi, M. Moridsadat, A. Tofini, et al., "Polymer Modulators in Silicon Photonics: Review and Projections," *Nanophotonics* 11, no. 17 (2022): 3855–3870.

21. L. Alloatti, R. Palmer, S. Diebold, et al., "100 GHz Silicon–Organic Hybrid Modulator," *Light: Science & Applications* 3, no. 5 (2014): e173.

22. A. Rahim, A. Hermans, B. Wohlfeil, et al., "Taking Silicon Photonics Modulators to a Higher Performance Level: State-of-the-art and a Review of new Technologies," *Advanced Photonics* 3, no. 2 (2021) 024003.

23. H. Deng and W. Bogaerts, "Pure Phase Modulation Based on a Silicon Plasma Dispersion Modulator," *Optics Express* 27, no. 19 (2019): 27191.

24. H. Deng, J. Zhang, E. Soltanian, et al., "Single-Chip Silicon Photonic Engine for Analog Optical and Microwave Signals Processing," *Nature Communications* 16, no. 1 (2025): 1–10.

25. L. Van Iseghem, E. Picavet, A. Y. Takabayashi, et al., "Low Power Optical Phase Shifter Using Liquid Crystal Actuation on a Silicon Photonics Platform," *Optical Materials Express* 12, no. 6 (2022): 2181.

26. P. Edinger, A. Y. Takabayashi, C. Errando-Herranz, et al., "Silicon Photonic Microelectromechanical Phase Shifters for Scalable Programmable Photonics," *Optics Letters* 46, no. 22 (2021): 5671.

27. M. Nedeljkovic, R. Soref, and G. Z. Mashanovich, "Free-Carrier Electrorefraction and Electroabsorption Modulation Predictions for Silicon Over the 1-14-μm Infrared Wavelength Range," *IEEE Photonics Journal* 3, no. 6 (2011): 1171–1180.

28. B. Hraimel, X. Zhang, W. Jiang, et al., "Experimental Demonstration of Mixed-Polarization to Linearize Electro-Absorption Modulators in Radio-Over-Fiber Links," *IEEE Photonics Technology Letters* 23, no. 4 (2011): 230–232.

29. K. Van Gasse, J. Verbist, H. Li, et al., "Silicon Photonics Radio-Over-Fiber Transmitter Using GeSi EAMs for Frequency up-conversion," *IEEE Photonics Technology Letters* 31, no. 2 (2019): 181–184.

30. W. Bogaerts, P. D. Heyn, T. V. Vaerenbergh, et al., "Silicon Microring Resonators," *Laser & Photonics Reviews* 6, no. 1 (2012): 47–73.

31. C. G. Bottenfield and S. E. Ralph, "High-Performance Fully Integrated Silicon Photonic Microwave Mixer Subsystems," *Journal of Lightwave Technology* 38, no. 19 (2020): 5536–5545, https://doi.org/10.1109/JLT.2020.2990693.

32. J. Yao, "Microwave photonics," *Journal of Lightwave Technology* 27, no. 3 (2009): 314–335.

33. J. E. Proesel, M. Meghelli, C. W. Baks, et al., "Nanosecond-Scale Shift-and-Dump Mach–Zehnder Switch," *Optics Letters* 44, no. 18 (2019): 4614–4616.

34. P. A. Morton, J. B. Khurgin, and M. J. Morton, "All-Optical Linearized Mach-Zehnder Modulator," *Optics Express* 29, no. 23 (2021): 37302.

35. Y. Zhao, J. Li, Z. Xiang, and J. Liu, "A Design of All-Optical Integrated Linearized Modulator Based on Asymmetric Mach-Zehnder Modulator," *Photonics* 10, no. 3 (2023): 229.

36. C. Catalá-Lahoz, M. Merklein, C. K. Lai, et al., "On-Chip Stimulated Brillouin Scattering to Linearize a Dual-Parallel Mach–Zehnder Modulator," *Journal of Lightwave Technology* 43, no. 11 (2025): 5244–5251.

37. Y. Zhang, X. Chen, L. Van Iseghem, et al., "General-Purpose Hexagonal Programmable Photonic Integrated Circuit with a >30 GHz Free Spectral Range," *Laser and Photonics Reviews* 20, no. 10 (2026): e02270, https://doi.org/10.1002/lpor.202502270.

Supporting Information

Additional supporting information can be found online in the Supporting Information section.

Supporting File: lpor71316-sup-0001-SuppMat.pdf.